Geophysical Journal International

Geophys. J. Int. (2011) **187,** 959–968 doi: 10.1111/j.1365-246X.2011.05189.x

Fault slip distribution and fault roughness

Thibault Candela,[1] François Renard,[1,2] Jean Schmittbuhl,[3] Michel Bouchon[1] and Emily E. Brodsky[4]

[1] *ISTerre, CNRS, University Joseph Fourier–Grenoble I, OSUG, BP* 53, 38041 *Grenoble, France. E-mail: Thibault.Candela@ujf-grenoble.fr*
[2] *Physics of Geological Processes, University of Oslo, Oslo, Norway*
[3] *UMR* 7516, *Institut de Physique du Globe de Strasbourg, Strasbourg, France*
[4] *Department of Earth and Planetary Sciences, University of California–Santa Cruz, Santa Cruz, CA* 95064, *USA*

Accepted 2011 August 9. Received 2011 July 5; in original form 2010 September 8

SUMMARY

We present analysis of the spatial correlations of seismological slip maps and fault topography roughness, illuminating their identical self-affine exponent. Though the complexity of the coseismic spatial slip distribution can be intuitively associated with geometrical or stress heterogeneities along the fault surface, this has never been demonstrated. Based on new measurements of fault surface topography and on statistical analyses of kinematic inversions of slip maps, we propose a model, which quantitatively characterizes the link between slip distribution and fault surface roughness. Our approach can be divided into two complementary steps: (i) Using a numerical computation, we estimate the influence of fault roughness on the frictional strength (pre-stress). We model a fault as a rough interface where elastic asperities are squeezed. The Hurst exponent H_τ, characterizing the self-affinity of the frictional strength field, approaches $H_\tau = H_{//} - 1$, where $H_{//}$ is the roughness exponent of the fault surface in the direction of slip. (ii) Using a quasi-static model of fault propagation, which includes the effect of long-range elastic interactions and spatial correlations in the frictional strength, the spatial slip correlation is observed to scale as $H_s = H_\tau + 1$, where H_s represents the Hurst exponent of the slip distribution. Under the assumption that the origin of the spatial fluctuations in frictional strength along faults is the elastic squeeze of fault asperities, we show that self-affine geometrical properties of fault surface roughness control slip correlations and that $H_s = H_{//}$. Given that $H_{//} = 0.6$ for a wide range of faults (various accumulated displacement, host rock and slip movement), we predict that $H_s = 0.6$. Even if our quasi-static fault model is more relevant for creeping faults, the spatial slip correlations observed are consistent with those of seismological slip maps. A consequence is that the self-affinity property of slip roughness may be explained by fault geometry without considering dynamical effects produced during an earthquake.

Keywords: Fourier analysis; Friction; Dynamics and mechanics of faulting.

GJI Seismology

1 INTRODUCTION

The increasing resolution of near-field strong ground motion records gives now a clear evidence of the spatio-temporal complexity of the rupture process. Even if different kinematic inversions for the same earthquake show discrepancies, images of the spatial and temporal evolution of coseismic slip on fault planes provide compelling evidence that fault displacement is spatially variable at all resolvable scales (Mai & Beroza 2002; Lavallée & Archuleta 2005). Seismic sources have been shown to present large heterogeneities in the coseismic slip and the rupture velocity (Archuleta 1984; Brune 1991; Cotton & Campillo 1995). The origin of this complexity is still poorly understood and might come either from the geometric irregularity of the fault surface and compositional heterogeneities (Mai & Beroza 2002), or dynamical effects (e.g. Cochard & Madariaga 1994).

In addition, in their extended analysis of spatial correlations of slip maps for 44 earthquakes, Mai & Beroza (2002) found that the heterogeneous slip distribution follows a self-affine regime characterized by an average value of the slip roughness exponent close to those of recent statistical scaling analyses of high resolution topography measurements of natural fault surfaces (Renard *et al.* 2006; Candela *et al.* 2009). Even if this similar geometrical complexity between slip maps and natural fault surfaces may suggest that both are associated, whether the observed slip patterns may reflect the underlying frictional or geometrical properties of the fault, or whether these are separate effects, remains to be addressed. The aim of this work is to propose an approach, which demonstrates that a

controlling parameter of the spatial slip correlations is related to the scaling properties of the topography of the slip surface (i.e. fault roughness).

In the following, we present new analysis of the spatial correlations of seismological slip maps (Section 2) and new data of fault surface roughness (Section 3), illuminating their identical self-affine exponent. In Section 4, we present our model that can be divided in two parts. First, we link the shear strength field distribution (prestress) to the roughness of the fault plane using a numerical computation of the transformation of fault asperities (including the broad range of asperity size as suggested by the self-affine property of natural fault surfaces) when submitted to a normal load. Only elastic deformation of the topography is considered, which is dominant at large scales, while the friction coefficient is held constant (i.e. Byerlee's criterion). Secondly, using a quasi-static numerical model of fault propagation, which includes the effects of long-range elastic interactions, we study the influence of the shear strength field distribution, provided by the first step of our model, on the resulting slip distribution. Finally, we compare our numerical slip distribution with that of seismological slip maps on active faults.

2 SELF-AFFINE CORRELATIONS OF SEISMOLOGICAL SLIP FIELDS

Let first recall some definitions related to the scaling properties of a rough signal. A self-affine 1-D profile (Fig. 1) remains unchanged under the scaling transformation $\delta x \rightarrow \lambda \delta x, \delta z \rightarrow \lambda^H \delta z$ (Meakin 1998). Here, δx is the coordinate along the 1-D profile and δz is the slip or roughness amplitude in the framework of our study. As a consequence the large-scale slope along a profile scales as $s = \delta z / \delta x \propto \delta x^{H-1}$(Schmittbuhl *et al*. 1995a). In the particular case where $H = 1$, the profile is called self-similar. Therefore, if a profile obeys to a self-similar description, a small portion of the profile, when magnified isotropically, has a statistically identical appearance to a larger part of the profile. Conversely, as opposed to self-similar surfaces, a self-affine profile with $0 \leq H \leq 1$ is flatter at large scales but still includes a large variety of amplitudes of small-scale asperities. Therefore, if a profile is best-fitting with a self-affine model, different magnification factors will be needed for the directions parallel and perpendicular to the profile for a small portion of the profile to appear statistically similar to the entire profile (Fig. 1).

Theoretical studies of extended source earthquake models describe heterogeneous slip distributions on fault planes (Andrews 1980; Frankel 1991; Herrero & Bernard 1994) following a self-similar behaviour characterized by $H_s = 1$, with H_s the Hurst exponent of the spatial distribution. However, in their extended analysis of spatial correlations of slip maps for 44 earthquakes, Mai & Beroza (2002) found that the heterogeneous slip distribution follows a self-affine regime characterized by an average value $H_s = 0.71 \pm 0.23$, independently of moment magnitude or source dimensions. In support of these findings, Causse *et al.* (2010) have shown that kinematic inversions methods are relevant tools to retrieve the slip roughness even if the smoothing constraints used to stabilize the inversion lead to a slight underestimation of the slip spectrum corner wavenumber. The observation that $H_s < 1$ implies a larger short-scale variability of slip than for the self-similar model, and indicates that this model may not apply to explain the current knowledge on slip maps.

In the spirit of the analysis of Mai & Beroza (2002), we have examined the scaling heterogeneities of several slip fields extracted from finite-source rupture models (http://www.seismo.ethz.ch/srcmod), and selected 10 of them with a frequency content sufficiently large for a Fourier analysis (see also Table 1).

The Hurst exponent H_s can be estimated from the Fourier power spectrum, which follows a power law for a 1-D self-affine profile (Barabasi & Stanley 1995; Meakin 1998). For each parallel profile extracted in the horizontal direction (or strike direction) of a slip map (Fig. 2), the Fourier power spectrum $P(k)$, that is, the square of the modulus of the Fourier transform, is calculated as a function of the wavenumber k. Then the spectrum of the entire surface is calculated by stacking and averaging all 1-D Fourier transforms to reduce the noise associated with individual profiles. When plotting the power spectrum as a function of wavenumber in a log–log space, a self-affine function reveals a linear slope, which is itself a function

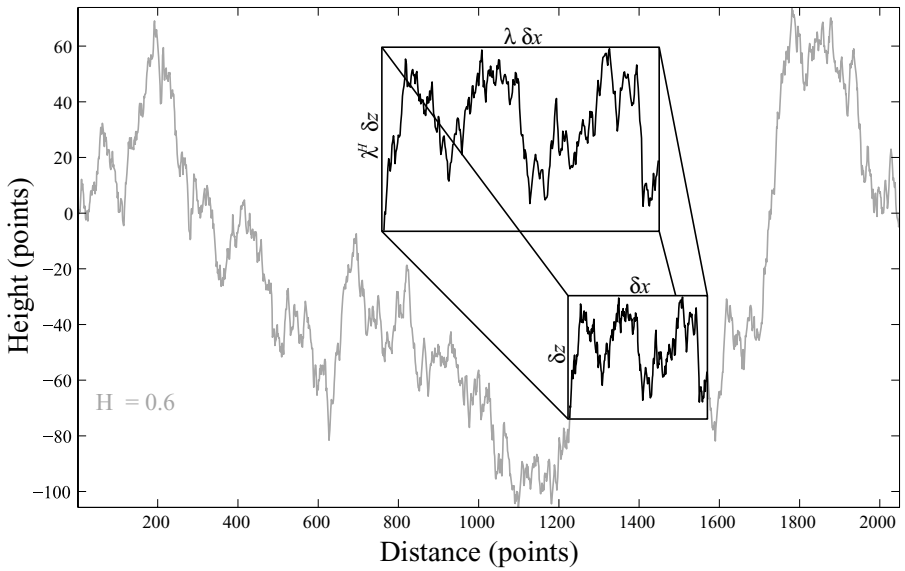

Figure 1. Representative 1-D synthetic self-affine profile computed with a Hurst exponent equal to 0.6. We used a Fourier-based method to simulate the self-affine profile, as performed by Candela *et al.* (2009). Inset: magnified portion of the profile, which has a statistically similar appearance to the entire profile when using the rescaling transformation $\delta x \rightarrow \lambda \delta x, \delta z \rightarrow \lambda^H \delta z$.

Table 1. Selected slip models.

No.	Location	Date	[a]Frequency range (m^{-1})	H_s	H_s[b]	M_w	Reference
1	Chi-Chi (Taiwan)	1999 September 20	$[10^{-5}–4{\cdot}10^{-4}]$	0.54	0.66	7.61	*Zeng and Chen (2001)*
2	Loma Prieta	1989 October 18	$[2{\cdot}10^{-5}–4{\cdot}10^{-4}]$	0.74	0.72	6.98	*Zeng and Anderson (2000)*
3	Loma Prieta	1989 October 18	$[2{\cdot}10^{-5}–4{\cdot}10^{-4}]$	0.56	0.50	6.95	*Beroza (1991)*
4	Kobe	1995 January 17	$[10^{-5}–4{\cdot}10^{-4}]$	0.64	0.22	6.90	*Zeng and Anderson (2000)*
5	Kobe	1995 January 17	$[10^{-5}–4{\cdot}10^{-4}]$	0.59	0.40	6.99	*Sekiguchi et al. (1996)*
6	Imperial Valley	1979 October 15	$[2{\cdot}10^{-5}–4{\cdot}10^{-4}]$	0.51	0.66	6.35	*Zeng and Anderson (2000)*
7	Northridge	1994 January 17	$[4{\cdot}10^{-5}–4{\cdot}10^{-4}]$	0.59	0.73	6.71	*Zeng and Anderson (2000)*
8	Landers	1992 June 6	$[10^{-5}–4{\cdot}10^{-4}]$	0.65	0.72	7.20	*Zeng and Anderson (2000)*
9	Denali (Alaska)	2002 November 3	$[2{\cdot}10^{-6}–4{\cdot}10^{-4}]$	0.54		7.91	*Oglesby et al. (2004)*
10	Denali (Alaska)	2002 November 3	$[2{\cdot}10^{-6}–4{\cdot}10^{-4}]$	0.52		7.87	*Asano et al. (2005)*
Average				0.59	0.58		

[a]The frequency range corresponds to upper and lower limits of wavenumbers used for fitting in Fig. 2.
[b]Roughness exponents of slip maps obtained by Mai & Beroza (2002).

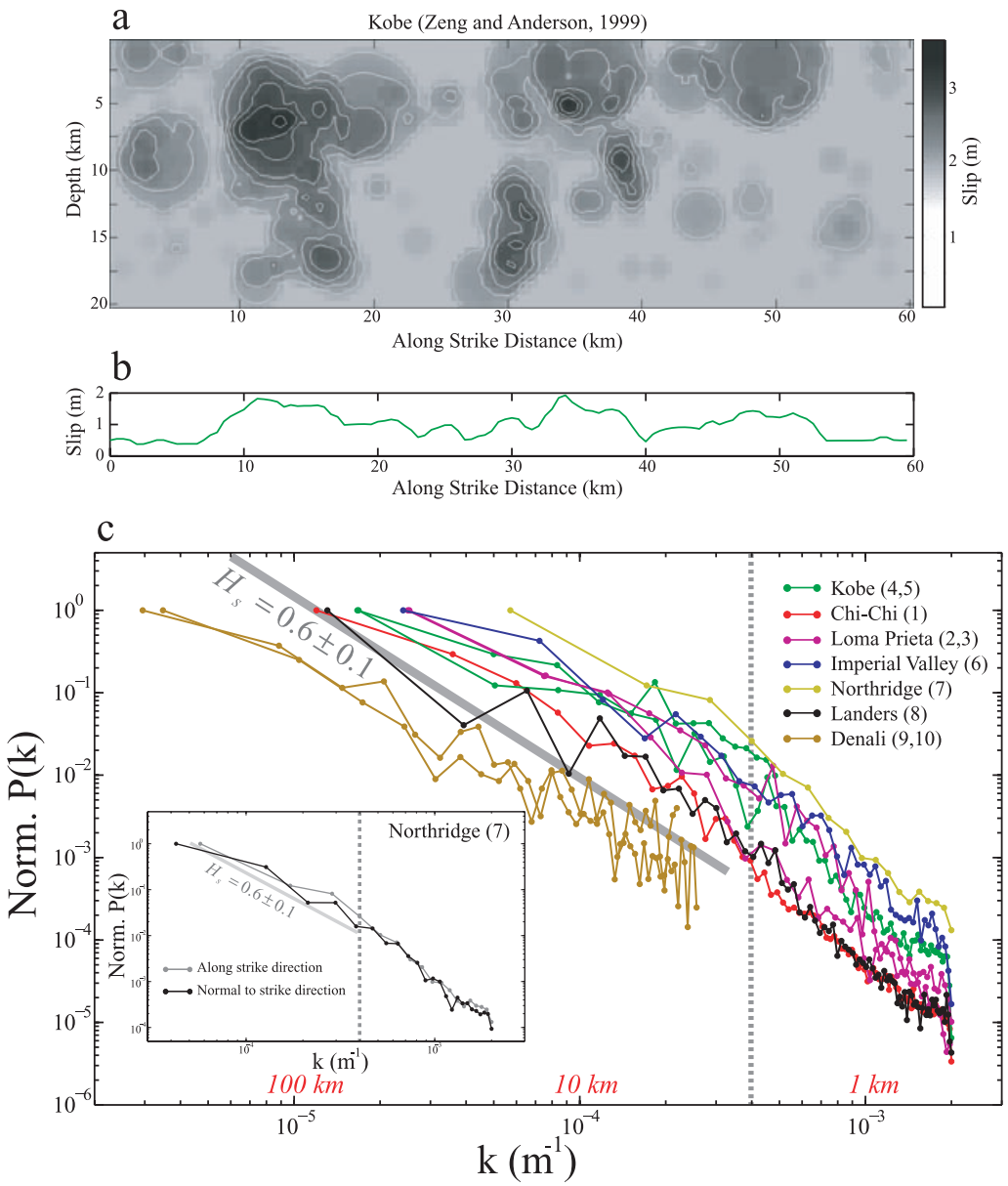

Figure 2. Analyses of the roughness of several seismological slip distributions. (a) Example of one of the 10 slip maps analysed (Table 1) derived by Zeng & Anderson (2000) for the Kobe earthquake, and illustrating the spatial variability of slip on the rupture plane. (b) Representative slip profile extracted from the Kobe earthquake map. (c) Normalized Fourier power spectra of the horizontal (or strike direction) slip profiles of the 10 slip maps analysed. Inset: illustration for the Northridge earthquake of the identical self-affine regime in the strike direction and perpendicular to it.

of H_s through $P(k) = Ck^{-1-2H_s}$. The power-law exponent of the spectrum, $-1 - 2H_s$, describes how the roughness changes with scale, whereas the intercept C, also called the pre-factor of the power law, fixes the steepness or roughness of the surface at a reference scale (Mandelbrot 1983, p. 350; Power & Tullis, 1991), and both parameters are necessary and sufficient to describe a self-affine model.

As we focus our analysis on the slope of the spectrum and to allow a better comparison of each power spectrum, Fig. 2 displays the normalized power spectra of the 10 slip fields selected along strike direction (Table 1). In this figure, each Fourier spectrum is normalized by its maximum power. Even if the direction normal to strike corresponds to the average slip direction for normal or reverse faults, this direction is less extended than along strike and contains most of the time insufficient frequency content for a Fourier spectral analysis. However, as suggested by Mai & Beroza (2002) and our analysis on the Northridge earthquake slip map (inset on Fig. 2), which contains a sufficient frequency content in the direction normal to strike, both directions have identical self-affine exponents. Finally, at large scales (above approximately 3 km), that is, above the effect of the spatial smoothing applied in the slip inversion, we find a self-affine behaviour characterized by an average value of $H_s = 0.6 \pm 0.1$ which is very close to the average roughness exponent calculated by Mai & Beroza (2002) for these 10 selected slip maps (Table 1) and falls within the range proposed in their extended analysis of spatial correlations of 44 slip maps.

3 FAULT SURFACE ROUGHNESS

3.1 Self-affine properties of fault surfaces

High-resolution relocations of earthquakes using the multiplet technique have shown linear spatial distributions of microearthquakes along major faults in California (Rubin *et al.* 1999). This pattern has been interpreted as resulting from the presence of an organized large-scale fault roughness (asperities) resisting slip (Schaff *et al.* 2002). However, despite recent progress in seismology, the imaging of fault planes over a large range of scales at depth is not yet available. A quasi-unique access to high-resolution description of the fault plane comes from exhumed fault scarp observations. This requires, of course, that the main morphological patterns of faults mapped at the surface of the Earth persist at least across the seismogenic zone.

Owing to technical limitations, the roughness of several fault planes has been studied mainly using 1D profilometry (Power *et al*. 1987). From these pioneer measurements, natural fault roughness has been shown to be scale-invariant with a self-similar (Power *et al.* 1987, 1988; Power & Tullis 1991) or self-affine character (Schmittbuhl *et al.* 1993; Lee & Bruhn, 1996).

As pointed out by Power *et al.* (1987), there is a significant limitation in studying such roughness profiles, both because of intrinsic heterogeneity of the fault surfaces that may have existed at the time of faulting, and because later degradation of the surface by weathering may introduce variability and errors in the determination of the slope of the spectrum. This may explain why their studies (i) did not have access to slight variations of the slopes and (ii) concluded on the presence of an 'average' self-similar regime (e.g. Power & Tullis 1991).

With the recent development of high-resolution distance meters, it is now possible to use accurate statistical approaches to quantify fault roughness. Indeed, portable 3-D laser scanners [also called Light Detection And Ranging (LiDAR)] allow mapping fault surface outcrops over scales of millimetres to several tens of metres (Renard *et al.* 2006; Sagy *et al.* 2007; Candela *et al.* 2009; Brodsky *et al.* 2011). The accuracy of the measurements enables a reliable quantification of the data. Renard *et al*. (2006) and Candela *et al*. (2009) demonstrated precisely the self-affine properties of fault topography using ground-based LiDAR and laboratory profilometers. These studies, using two different and independent signal processing tools, validate the preliminary results of Schmittbuhl *et al.* (1993) and Lee & Bruhn (1996), and indicate that the various faults are characterized by an approximately identical self-affine geometry.

In the following paragraph, we use a technique based on Fourier power spectrum, as previously presented for slip correlations analysis and whose reliability and accuracy has been previously tested (Schmittbuhl *et al.* 1995b; Candela *et al*. 2009) to investigate the scaling properties of fault surfaces, and confirm the self-affine model.

3.2 Scaling properties of the Corona Heights Fault, California

We present new roughness data obtained on a fault localized in the Castro Area of San Francisco (Corona Heights, 37.76°N, 122.43°W), that crosscuts the brown Franciscan cherts, and where a post-1906 earthquake aggregate quarry has been transformed into a playground and pet cemetery. The relatively recent exposure of the fault (Fig. 3a) and the high resistance of cherts to weathering allow excellent preservation of the slip surface itself. This fault has a mainly strike-slip component, witnessed by large elongated bumps and depressions, associated with linear striations of smaller size observed at all scales down to the resolution of the measurement devices. We emphasize that the fault surface is characterized by an anastomosing network of highly polished, slickenlined surfaces, which might have been active during different episodes of faulting and might have accumulated various displacements.

At the field scale, a LiDAR apparatus (HDS3000; Leica, www.leica-geosystems.com/hds) was used to acquire six digital elevation models (DEM, or fault patch) of the fault roughness at a spatial length scale resolution of 5 mm and with a height resolution of approximately 2 mm (Fig. 3b). At the laboratory scale, the roughness of two slip planes (Fig. 3c) was characterized using a laser profilometer (Méheust 2002; Schmittbuhl *et al*. 2008) with horizontal increments of 20μm and a vertical resolution better than 1μm. We used also a White Light Interferometer (WLI) microphotography (Wyko 2000 Surface Profiler; Veeco, www.veeco.com), giving access to a micrometre spatial length scale resolution for an estimated height resolution close to 3nm of two slip surface samples (Fig. 3d). Note that even if our LiDAR surface measurements were acquired at a spatial length scale resolution of 5 mm, total power estimates of the surfaces are accurate only between 10—and 0.05 m scales. In other words, for wavelengths below 5 mm, the fault surfaces we scanned with the LiDAR are so smooth that at this small scale, their spectral power falls in the range of those of the flat plate we use as a planar reference surface (Fig. 4). In contrast, the noise level inherent in the laboratory scale laser profilometer and the WLI is much lower, well below the magnitude of the surface topography (Fig. 4). For this reason, the laser profilometer and WLI data can be considered to be essentially noise-free.

Each fault surface, LiDAR measurement produces a matrix of millions of points from which 1-D profiles in any direction can be extracted (Fig. 4). To compare fault surface spatial correlations with that of the seismological slip maps, we focus our Fourier transform

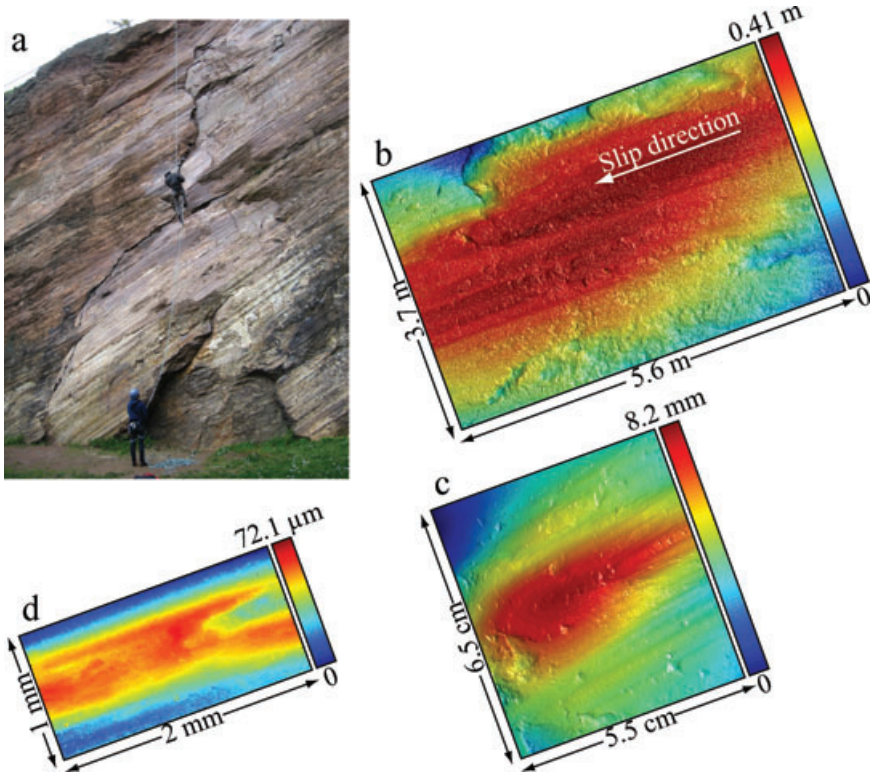

Figure 3. Surface topography of the Castro Area fault (Corona Heights, San Francisco). (a) The fault surface consists of many discrete slip surfaces at all scales. (b) Example of fault surface topography measured using a LiDAR, and represented as a colour-scale digital elevation model (DEM). The measurements were performed on a roughly regular grid with spatial resolution ~ 0.5 cm $\times$ 0.5 cm,which contains $\sim$ 2000, 000 points, and then averaged (bilinear interpolation) on a coarser grid to obtain the final model. The resolution of the elevation is less than 1 cm. (c) DEM of a hand sample, scanned with a laboratory laser profilometer. The surface contains 4000 $\times$ 4000 points on a regular grid with spatial resolution 20 $\times$ 20 μm^2 and elevation resolution less than 10 μm. (d) Example of a DEM obtained with white light interferometry, that contains 3000 $\times$ 3000 points on a regular grid and gives access to a micrometer height resolution.

analysis along the slip direction. Power spectra of the individual profiles (with roughly identical slopes but various intercepts) were stacked and averaged to form the power spectrum of the entire fault patch (see inset (a) on Fig. 4). In other words, for each fault patches at every scales (LiDAR, laser profilometer and WLI), power spectral estimates with regularly spaced wavenumbers were obtained by averaging the power spectra of the individual profiles in a geometric progression. Finally, at each scales (LiDAR, laser profilometer and WLI), one average spectrum is computed from the individual power spectra of every fault patches (see Fig. 4).

Following the method of Power & Durham (1997) to estimate the uncertainty in the average spectral values obtained for each device, which comes from Bendat & Piersol (1986), a one sigma confidence interval for the spectral power is given by $\frac{\sqrt{n_s}\hat{P}(k)}{\sqrt{n_s}+1} \leq P(k) \leq \frac{\sqrt{n_s}\hat{P}(k)}{\sqrt{n_s}-1}$ with $n_s(k) = n_y \Delta y k + 1$, where $P(k)$ and $\hat{P}(k)$ are, respectively, the actual and calculated spectral power; n_y and n_s are, respectively, the total number of profiles spaced a distance Δy apart perpendicular to the profile direction and the number of independent profiles, used to calculate $\hat{P}(k)$. Note that n_s depends on scale. For the large wavenumber end of the average spectra of each device, there are many more independent estimates of the total spectral power, and hence the error estimate is smaller than at the largest scales (see Fig. 4).

It is worth pointing out that when we compute the scaling from the LiDAR measurements, we average the power spectra of all individual rough profiles extracted from the surface. Each profile has a different intercept, but the average gives one specific intercept. At a lower length scale, with another device (i.e. laser profilometer or WLI), we select one subregion that has one given intercept among the whole population that we explored at larger scale (i.e. with the LiDAR) and that is not necessarily equal to the average intercept of the large-scale measurements (see inset (b) on Fig. 4). Due to this vertical shift between the average spectra obtained for each device, Hurst exponents are calculated separately, and are, respectively: 0.65 ± 0.05, 0.62 ± 0.05, 0.62 ± 0.03 for the LiDAR, laser profilometer and the WLI. Finally, our results highlight a self-affine regime in the slip direction characterized by $H_{//} = 0.63 \pm 0.05$ (referred to $H_{//} = 0.6$ afterwards), over approximately six decades of length scales (Fig. 4), excluding several regimes (with different roughness exponents) bounded by characteristic scales.

The compiled results of this analysis and previous works (Schmittbuhl *et al*. 1993; Lee & Bruhn 1996; Renard *et al*. 2006; Candela *et al*. 2009) clearly show that, despite different geological settings (various accumulated displacement, host rock and slip movement), a unique self-affine exponent may describe accurately the geometry of fault roughness along the slip direction. The fact that the fault studied was exhumed from shallow depth (<5 km), implies that (i) its topography has only recorded the propagation and termination of hypothetic major earthquakes ruptures that initiate at greater depths and (ii) it is difficult to identify irrefutable coseismic slip markers (as melt products). However, it is worth noting that in a recent work (Bistacchi *et al.* 2011), the same self-affine regime was found for the Gole Larghe Fault Zone (Italian Alps) where the conditions

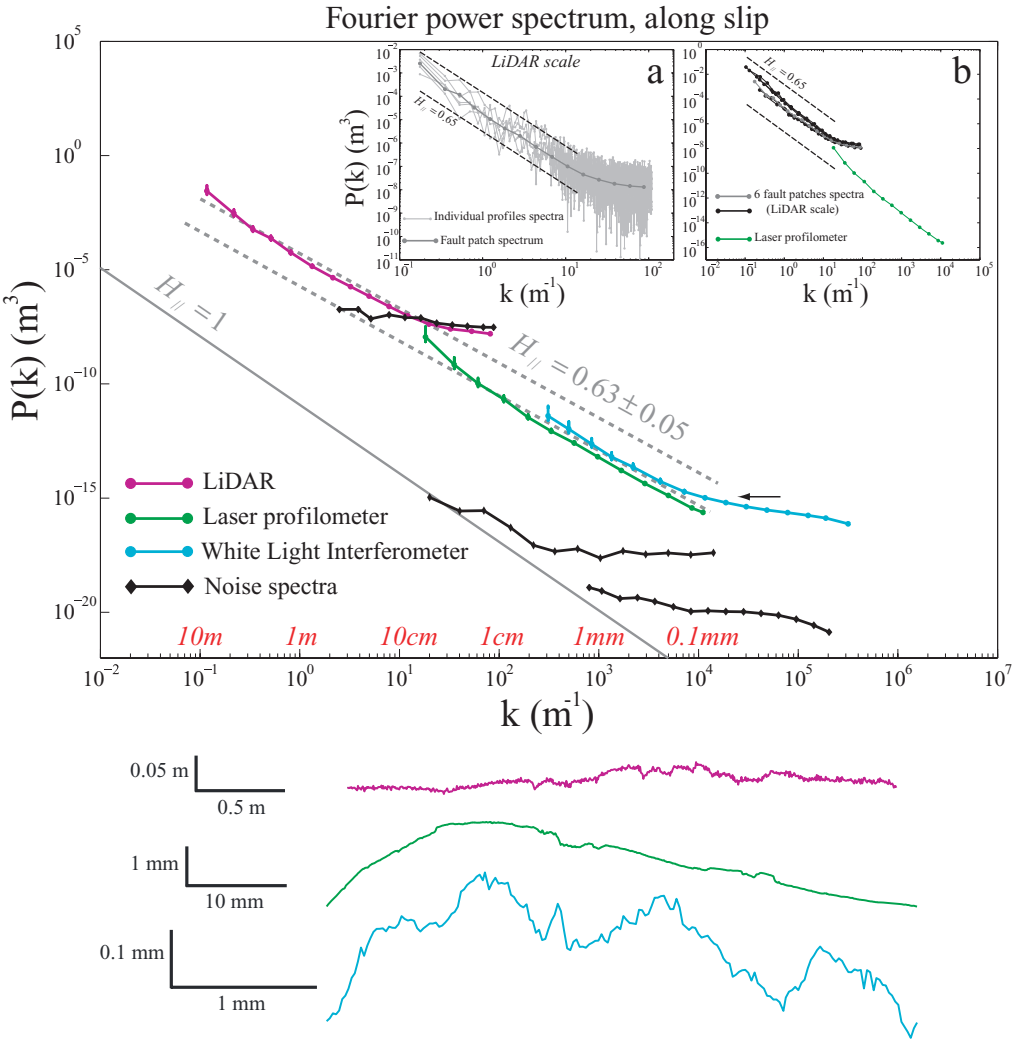

Figure 4. Roughness analysis of the Castro Area Corona Heights fault surface along the slip direction. Top panel: Average Fourier power spectra obtained from each device (LiDAR, laser profilometer and WLI) covering six decades of spatial wavelengths. Error bars with 68 per cent confidence interval (one sigma) are shown. Power-law fits (dashed grey lines) with a roughness exponent $H_{//} = 0.63 \pm 0.05$, connecting the field and laboratory data are shown on plot for eye guidance. The spectral power levels of our natural fault roughness data fall at a vertical higher position than the noise spectra calculated for each device scanning smooth, planar reference surfaces. The black arrow indicates the lower limit for the fit performed at the WLI scale. Inset: (a) Example of the power spectrum of one LiDAR fault patch obtained by scanning and averaging in a geometric progression several thousands power spectra of individual profiles (here only five spectra are displayed). Note the intercepts range of spectra performed from each individual profiles highlighted by the two dashed dark power laws. (b) Graph gathering the average laser profilometer spectrum with the six Fourier power spectra obtained at the LiDAR scale. Note that the average laser profilometer spectrum falls in the range of intercepts (underlined by the two dashed dark power law) sampled by the whole population of the individual profiles that we explore at the LiDAR scale. Bottom panel: Representative profiles extracted from DEM obtained with each device (see Fig. 3) and plotted at the same level of vertical exaggeration.

of seismogenic nucleation depths have been sampled and where pseudo-tachylytes were found (Di Toro & Pennacchioni 2005). One may conclude that the presented self-affine geometrical properties characterized by a unique Hurst exponent represent a global feature of natural fault surfaces and might be preserved at depth.

4 FROM FAULT GEOMETRY TO THE SPATIAL DISTRIBUTION OF SLIP

4.1 Correlation between the pre-stress field and fault roughness (asperity squeeze model)

Schmittbuhl *et al*. (2006) have proposed that heterogeneities of the stress field are dominated by intrinsic fault properties and are weakly sensitive to dynamical stress fluctuations due to earthquake propagation since spatially persistent before and after the rupture event (at least at large scales). Their model, based on the studies of Hansen *et al.* (2000) and Batrouni *et al*. (2002), consists of a boundary element method that describes the full normal contact between two facing elastic self-affine rough surfaces unmated with spatially correlated asperities. This model disregards plastic processes like rock fragmentation, and focuses on elastic deformation of the topography, which is the dominant mode at large scales. It follows that when the loading is sufficient to suppress the fault morphology roughness and transform it into a normal stress roughness along a smooth plane, the Hurst exponent H_σ, characterizing the self-affinity of the normal stress field (the initial or pre-stress field before a rupture event), approaches: $H_\sigma = H_{//} - 1$, where $H_{//}$ represents the Hurst exponent of the fault surface morphology under exposure condition (no normal stress). This relationship arises

from the fact that, for an elastic material, the stress field is related to the first derivative of the displacement field. If we use our estimate of the Hurst exponent of the fault morphology $H_{//} = 0.6$, we obtain that the Hurst exponent of the normal stress field is: $H_\sigma = -0.4$.

4.2 A quasi-static heterogeneous slip distribution model

We use a quasi-static 3-D fault model, detailed by Perfettini *et al.* (2001), which accounts for long-range elastic interactions. Perfettini *et al.* (2001) have examined the influence of spatial heterogeneities of frictional strength on the slip distribution along a creeping fault. In this model, slip fluctuates spatially because of pinning on local asperities (heterogeneities of frictional strength). Depinning from these asperities involves local instabilities. When the elastic coupling is small, the motion is controlled by individual asperities. Conversely, for strong elastic coupling, that is, weak pinning, asperities interact because of elasticity and the dynamics becomes global.

In distinction to the study of Perfettini *et al.* (2001), where a uniform random distribution of frictional strength was used to characterize a heterogeneous static pre-stress field, we consider here, also a disorder of the frictional strength (or shear strength) but spatially correlated and controlled by a self-affine exponent H_τ. We propose to link the Hurst exponent of the shear strength H_τ to that of the normal stress H_σ on the basis of a local Byerlee criterion: $\tau_c = \mu\sigma_n$ with $\mu = 0.6$. Because of the linearity between the shear strength and the normal stress, both are expected to exhibit the same scaling leading to: $H_\tau = H_\sigma = H_{//} - 1$. With our estimate of $H_{//} = 0.6$, we obtain$H_\tau = -0.4$.

4.2.1 Numerical model

In this paragraph, we briefly list the main characteristics and assumptions of the quasi-static numerical fault model, based on the study of Perfettini *et al.* (2001). We consider a simple elastic model of rupture along a fault plane located at $z = 0$ through an unbounded homogeneous elastic solid. The rupture propagates along the y direction.

The problem is then governed by a quasi-static scalar wave equation involving a 2-D displacement field $U(x, z; t)$, and the related shear traction across planes parallel to the crack is $\sigma(x, z; t)$. The actual slip $u(x; t) = U(x, 0^+; t) - U(x, 0^-; t)$ is the slip discontinuity across the fault plane and $\tau(x; t)$ denotes the associated perturbation of traction. We assume that slip occurs quasi-statically and neglect any dynamical effects. In that case, elastic waves are neglected, and the stress change $\tau(x; t)$, located at $y = 0$, and due to variations of slip discontinuity along the fault is given by (e.g. Cochard & Rice 1997)

$$\tau(x; t) = \frac{G}{2\pi} PV \int_L J(x - \xi)[u(\xi; t) - u(x; t)]\, \mathrm{d}\xi, \qquad (1)$$

where integration takes place over the fault of size L and PVindicates the principal value. The elastic kernel $J(x) = 1/x^2$ accounts for the long-range elastic interactions and G is the shear modulus. To avoid edge effects, we assume an L-periodic interface in the x direction such that the $1/x^2$ kernel in (1) transforms in $J_L(x) = (\pi/L)^2/\sin^2(\pi x/L)$.

To characterize locally the heterogeneous frictional properties along the interface, we balance $\tau(x; t)$ with a frictional strength that does not evolve with time $\eta_p(x; u(x; t))$. To mimic the spatial heterogeneities of the frictional strength previously described, their fluctuations are assumed to be spatially correlated with long-range correlations, that is, the frictional strength are controlled by a negative self-affine exponent $H_\tau = -0.4$. A uniform random distribution of the frictional strength (Perfettini *et al.* 2001) would correspond to $H_\tau = -1$ in two dimensions (Hansen *et al.* 2001). The correlation function of the frictional strength is assumed to behave as $\Gamma(x - x') \propto |(x - x')|^{2H_\tau}$ and in Fourier space $P(k) \propto k^{-2-2H_\tau}$.

At any time, the quasi-static motion of the fault has to satisfy: $\eta_p(x; u(x; t)) \geq \tau(x; t)$ for all points of the interface. The evolution of the system may be regarded as purely dissipative, that is, all the released energy being dissipated by frictional work (Fisher 1998).

The loading results from an imposed displacement. The system is discretized both in time and space. An elementary step (i.e. a time step) corresponds to the motion of only one segment for which a frictional strength $\eta_p(x; u(x; t))$ has been defined. At each step, the weakest segment is searched for (i.e. event-driven dynamics) by assuming that its location corresponds to the least shear traction required to advance the crack and slips by an elementary distance which is a fraction of the discretization length. The local driving force is locally updated according to the adopted self-affine distribution to follow the imposed disorder of the frictional strength. At that stage, the rupture front is locally unloaded and all the forces along the front line are modified according to a discretized form of eq. (1). The procedure is then repeated. The behaviour of the system is controlled by the competition between local fluctuations of the frictional strength and the effects of long-range elastics interactions.

Perfettini *et al.* (2001) have shown that three regimes of slip correlations exist depending on the ratio of the stress drop of a point that just slipped by an elementary distance and the root-mean-square (rms) of the frictional strength fluctuations. In the first regime, when the stress drop is much greater than the rms of the frictional strength fluctuations, the heterogeneities are not strong enough to pin the front, thus crack advance can never be arrested. Conversely, slip in the second regime is expected to have the same statistical distribution as the fluctuation of the frictional strength, because the magnitude of the elastic interactions (due to a small stress drop) is much smaller than the frictional strength heterogeneities. The third regime, on which we focus our study, is intermediate and the magnitude of the elastic interactions is comparable to the frictional strength variations. The interactions between frictional strength heterogeneities and elastic stress transfers lead to non-trivial spatio-temporal correlations of slips.

4.2.2 Results

In the numerical model, we let an initially flat slip front evolve with increasing displacement. In Fig. 5, the evolution of the crack-front line geometry during the transient regime is displayed, and corresponds to the spreading of slip over the whole length of the model, until slip correlations reach a stationary regime. For small increment of slip, the profile appears essentially flat (only correlated at small wavelengths), showing that the spatial correlations between successive slip distributions occur at small wavelengths. As slip increases, the activity zone spreads, and the profile appears correlated at all length scales when it reaches the system size. In other words, during the transient regime, the spreading of the activity is emphasized by the increase of the fluctuations of the crack-front line, which becomes rougher and rougher until a stationary geometry is reached. The spreading of the activity with increasing displacement results from two competing effects: long-range elastic interactions and frictional strength heterogeneities. The former tends to strongly

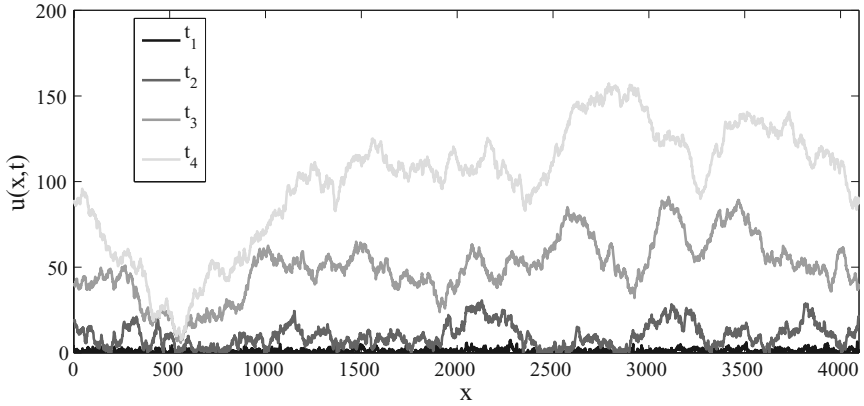

Figure 5. Evolution (bottom to the top) of the crack-front line geometry during the transient regime until the stationary state. The system size is 4096. Elementary slip of broken segment is taken in a uniform distribution [0.09; 0.11]. The shear modulus is set to 30 GPa. The average shear strength is 100 MPa with a root mean square deviation of 30 MPa. The Hurst exponent of the shear strength distribution is $H_\tau = -0.4$.

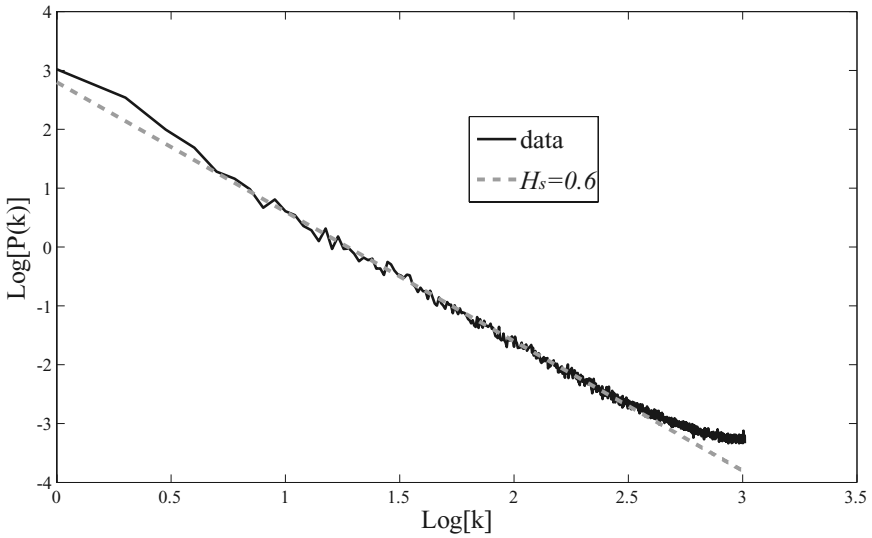

Figure 6. Power spectrum of the slip distribution in the statistically stationary regime, averaged over 7322 fronts taken each after 4096 iterations (3×10^7 iterations in total). The power-law fit provides an estimate of the Hurst exponent of the slip distribution: $H_s = 0.6$.

correlate slip laterally whereas the latter tends to pin the slip at one site.

The power spectrum of the slip distribution in the statistically stationary regime, averaged over many realizations of the rupture front, is shown in Fig. 6. As previously indicated, we have considered the case where frictional strength correlations are controlled by a self-affine exponent $H_\tau = -0.4$, which mimics the initial strength field along a fault. The Fourier power spectrum of the modelled fronts exhibits a power-law behaviour with a power exponent $\alpha = -2.2$, which indicates a self-affine behaviour with a Hurst exponent $H_s = 0.6$ ($\alpha = -2H_s - 1$, see Meakin 1998).

This result is consistent with that obtained for mode I ruptures by Schmittbuhl & Villote (1999), who studied the slow propagation of an interfacial mode I crack, including the effects of long-range elasticity and those of spatial correlations in the toughness of the interface. They obtained that the crack-front line correlations scale as $H_s = H_\tau + 1$ for any value of H_τ, which extends our particular case, $H_s = 0.6$ and $H_\tau = -0.4$, using the analogy between mode I fracture and shear rupture discussed in Schmittbuhl *et al.* (2003).

Finally, combining $H_\tau = H_{//} - 1$, that comes from the elastic squeeze of fault asperities, and $H_s = H_\tau + 1$, given by our numerical fault model, we obtain that $H_s = H_{//}$. In other words, we propose that the origin of the spatio-temporal complexity of the slip distribution could be related to geometrical properties of the fault. Considering two self-affine surfaces pressed together elastically and sheared, we have made the link between the 3-D fault roughness, which is perpendicular to the fault plane, and the 2-D slip roughness included in the fault plane.

5 DISCUSSION AND CONCLUSION

The elastic quasi-static squeeze model, as we have shown, provides a direct link between the stress field and the fault morphology developed during a long series of different rupture events. In that sense and using a quasi-static rupture model, our analysis provides a link between individual event slip and cumulative morphology of the fault.

Considering the two main assumptions made in our study (fluctuations of the stress field along the fault are dominated by fault properties and slip occurs quasi-statically), our results shed some lights on the influence of the fault surface roughness on the spatial slip distribution for creeping faults. Indeed, our work proposes a direct link between correlations in shear strength and slip distribution along the fault plane. Given that the origin of the spatial fluctuations of the shear strength (or initial stress) along faults is possibly the elastic squeeze of fault asperities, we therefore demonstrate that self-affine geometrical properties of fault surface roughness may control slip correlations.

Even if our quasi-static fault model is more adapted to creeping faults since inertia and wave effects, are neglected, it is worth noting that the self-affine spatial slip correlations observed in the quasi-static model are consistent with that of seismological slip maps for which dynamical effects are important. In other words, we showed that a quasi-static solution, which takes into account the geometrical irregularities of fault surface observed in the field, is in agreement with the seismological data, suggesting that dynamical effects produced during an earthquake could represented only a second-order effect. In this line of thoughts and as pointed out by Sammis *et al.* (1999), our results would support the hypothesis that the continuous slip on a creeping fault may result from a series of microevents related to breakage of asperities (such as the ones in the numerical model), and has the advantage of collectively gathering seismically active and creeping faults. However, it remains to use a complete elastodynamic description for this problem (Ramanathan & Fisher, 1997) to demonstrate that our solution is unique.

ACKNOWLEDGMENTS

This study was supported by the *Agence Nationale pour la Recherche* grants ANR-JCJC-0011–01 and ANR-SUPNAF. We thank Fabrice Cotton for fruitful discussions.

REFERENCES

Andrews, D.J., 1980. A stochastic fault model: 1. Static case, *J. geophys. Res.,* **85,** 3867–3877.

Archuleta, R., 1984. A faulting model for the 1979 Imperial Valley, California earthquake, *J. geophys. Res.,* **89,** 4559–4585.

Asano, K., Iwata, T. & Irikura, K., 2005. Estimation of source rupture process and strong ground motion simulation of the 2002 Denali, Alaska, earthquake, *Bull. seism. Soc. Am.,* **95**(5), 1701–1715.

Barabasi, A.-L. & Stanley, H.E., 1995. *Fractal Concepts in Surface Growth*. Cambridge University Press, New York.

Batrouni, G., Hansen, A. & Schmittbuhl, J., 2002. Elastic response of rough surfaces in partial contact, *Europhys. Lett.,* **60**(5), 724–730.

Bendat, J.S. & Piersol, A.G., 1986. *Random Data: Analysis and Measurement Procedures,* John Wiley, New York, 566pp.

Beroza, G.C., 1991. Near-source modeling of the Loma-Prieta earthquake – evidence for heterogeneous slip and implications for earthquake hazard, *Bull. seism. Soc. Am.,* **81**(5), 1603–1621.

Bistacchi, A., Griffith, W.A., Smith, S.A.F., Di Toro, G., Jones, R. & Nielsen, S., 2011. Fault roughness at seismogenic depths from LIDAR and photogrammetric analysis, *Pure appl. Geophys.,* doi:10.1007/s00024-011-0301-7.

Brodsky, E.E., Gilchrist, J.G., Sagy, A. & Colletini, C., 2011. Faults smooth gradually as a function of slip, *Earth planet. Sci. Lett.,* **302,** 185–193.

Brune, J., 1991. Seismic source dynamics, radiation and stress, *Rev. Geophys.,* **29,** 688–699.

Candela, T., Renard, F., Bouchon, M., Marsan, D., Schmittbuhl, J. & Voisin, C., 2009. Characterization of fault roughness at various scales: implications of three-dimensional high resolution topography measurements, *Pure. appl. Geophys.,* **166,** 1817–1851.

Causse, M., Cotton F. & Mai, P.M., 2010. Constraining the roughness degree of slip heterogeneity, *J. geophys. Res.,* **115,** B05304, doi:10.1029/2009JB006747.

Cochard, A. & Madariaga, R., 1994. Dynamic faulting under rate-dependent friction, *Pure. appl. Geophys.,* **142,** 419–445.

Cochard, A. & Rice, J.R., 1997. A spectral method for numerical elastodynamic fracture analysis without spatial replication of the rupture event, *J. Mech. Phys. Solids,* **45,** 1393–1418.

Cotton, F. & Campillo, M., 1995. Inversion of strong ground motion in the frequency domain: applications to 1992 Landers, California earthquake, *J. geophys. Res.,* **100,** 3961–3975.

Di Toro, G. & Pennacchioni, G., 2005. Fault plane processes and mesoscopic structure of a strong-type seismogenic fault in tonalites (Adamello batholith, Southern Alps), *Tectonophysics,* **402,** 55–80.

Fisher, D., 1998. Collective transport in random media: from superconductors to earthquakes, *Phys. Rep.,* **301,** 113–150.

Frankel, A., 1991. High-frequency spectral fall-off of earthquakes, fractal dimension of complex rupture, *b* value, and the scaling of strength on faults, *J. geophys. Res.,* **96,** 6291–6302, doi:10.1029/91JB00237.

Hansen, A., Schmittbuhl, J., Batrouni, G. & Oliveira, F.A., 2000. Normal stress distribution of rough surfaces in contact, *Geophys. Res. Lett.,* **27,** 3639–3643.

Hansen, A., Schmittbuhl, J. & Batrouni, G., 2001. Distinguishing fractional and white noise in one and two dimensions, *Phys. Rev. E,* **63,** doi:10.1103/PhysRevE.63.062102.

Herrero, A. & Bernard, P., 1994. A kinematic self-similar rupture process for earthquakes, *Bull. seism. Soc. Am.,* **84**(4), 1216–1288.

Lavallée, D. & Archuleta, R.J., 2005. Coupling of the random properties of the source and the ground motion for the 1999 Chi Chi earthquake, *Geophys. Res. Lett.,* **32,** doi:10.1029/2004GL022202.

Lee, J.J. & Bruhn, R.L., 1996. Structural anisotropy of normal fault surfaces, *J. Struct. Geol.,* **18,** 1043–1059.

Mai, P.M. & Beroza, G.C., 2002. A spatial random field model to characterize complexity in earthquake slip, *J. geophys. Res.,* **107,** doi:10.1029/2001JB000588.

Mandelbrot, B.B., 1983. *The Fractal Geometry of Nature,* W.H. Freeman, New York.

Meakin, P., 1998. *Fractals: Scaling and Growth Far from Equilibrium,* Cambridge University Press, New York.

Méheust, Y., 2002. Ecoulements dans les fractures ouvertes, *PhD thesis*, Univ. Paris VI and Ecole Normale Supérieure, Paris.

Oglesby, D.D., Dreger, D.S., Harris, R.A., Ratchkovski, N. & Hansen, R., 2004. Inverse kinematic and forward dynamic models of the 2002 Denali fault earthquake, Alaska, *Bull. seism. Soc. Am.,* **94**(6), S214–S233.

Perfettini, H., Schmittbuhl, J. & Vilotte, J., 2001. Slip correlations on a creeping fault, *Geophys. Res. Lett.,* **28**(10), 2133–2136.

Power, W.L. & Durham, W.B., 1997. Topography of natural and artificial fractures in granitic rocks: implications for studies of rock friction and fluid migration, *Int. J. Rock Mech. Min. Sci.,* **34,** 979–989.

Power, W.L. & Tullis, T.E., 1991. Euclidean and fractal models for the description of rock surface roughness, *J. geophys. Res.,* **96,** 415–424, doi:10.1029/90JB02107.

Power, W.L., Tullis, T.E., Brown, S.R., Boitnott, G.N. & Scholz, C.H., 1987. Roughness of natural fault surfaces, *Geophys. Res. Lett.,* **14,** 29–32.

Power, W.L., Tullis, T.E. & Weeks, J.D., 1988. Roughness and wear during brittle faulting, *J. geophys. Res.,* **93**(15), 268–278.

Ramanathan, S. & Fisher, D., 1997. Dynamics and instabilities of planar tensile cracks in heterogeneous media, *Phys. Rev. Lett.,* **79,** 877–880.

Renard, F., Voisin, C., Marsan, D. & Schmittbuhl, J., 2006. High resolution 3D laser scanner measurements of a strike-slip fault quantify its morphological anisotropy at all scales, *Geophys. Res. Lett.,* **33,** L04305, doi:10.1029/2005GL025038.

Rubin, A.M., Gillard, D. & Got, J.-L., 1999. Streaks of microearthquakes along creeping faults, *Nature,* **400,** 635–641.

Sagy A., Brodsky, E.E. & Axen, G.J., 2007. Evolution of fault-surface roughness with slip, *Geology,* **35,** 283–286.

Sammis, C.G., Nadeau, R.M. & Johnson, L.R., 1999. How strong is an asperity? *J. geophys. Res.,* **104,** 10 609–10 619, doi:10.1029/1999JB900006.

Schaff, D.P., Bokelmann, G.H.R., Beroza, G.C., Waldhauser, F. & Ellsworth, W.L., 2002. High-resolution image of Calaveras fault seismicity, *J. geophys. Res.,* **107,** doi:10.1029/2001JB000633.

Schmittbuhl, J. & Vilotte, J., 1999. Interfacial crack front wandering: influence of correlated quenched noise, *Physica A,* **270,** 42–56.

Schmittbuhl, J., Gentier, S. & Roux, R., 1993. Field measurements of the roughness of fault surfaces, *Geophys. Res. Lett.,* **20,** 639–641.

Schmittbuhl, J., Schmitt, F. & Scholz, C.H., 1995a. Scaling invariance of crack surfaces, *J. geophys. Res.,* **100,** 5953–5973.

Schmittbuhl, J., Vilotte, J.P. & Roux, S., 1995b. Reliability of self-affine measurements, *Phys. Rev. E,* **51,** 131–147.

Schmittbuhl, J., Delaplace, A., Maloy, K., Perfettini, H. & Vilotte, J., 2003. Slow crack propagation and slip correlations, *Pure appl. Geophys.,* **160,** 961–976, doi:10.1007/PL00012575.

Schmittbuhl, J., Chambon, G., Hansen, A. & Bouchon, M., 2006. Are stress distributions along faults the signature of asperity squeeze? *Geophys. Res. Lett.,* **33,** doi:10.1029/2006GL025952.

Schmittbuhl, J., Steyer, A., Jouniaux, L. & Toussaint, R., 2008. Fracture morphology and viscous transport, *Int. J. Rock. Mech. Min. Sci.,* **45,** 422–430.

Sekiguchi, H., Irikura, K., Iwata, T., Kakehi, Y. & Hoshiba, M., 1996. Minute locating of faulting beneath Kobe and the waveform inversion of the source process during the 1995 Hyogo-ken Nanbu, Japan, earthquake using strong ground motion records, *J. Phys. Earth,* **44**(5), 473–487.

Zeng, Y. & Anderson, J., 2000. Evaluation of numerical procedures for simulating near-fault long-period ground motions using Zeng method, *Report 2000/01 to the PEER Utilities Program,* available at http://peer.berkeley.edu

Zeng, Y.H. & Chen, C.H., 2001. Fault rupture process of the 20 September 1999 Chi-Chi, Taiwan, earthquake, *Bull. seism. Soc. Am.,* **91**(5), 1088–1098.